

In and out star formation in $z \sim 1.5$ quiescent galaxies from rest-frame UV spectroscopy and the far-infrared[★]

R. Gobat¹, E. Daddi², V. Strazzullo³, B. Garilli⁴, M. Mignoli⁵, Z. Ma⁶, S. Jin^{2,7}, C. Maraston⁸, G. Magdis^{9,10}, M. Béthermin¹¹, M. Cappellari¹², M. Carollo¹³, A. Cimatti¹⁴, C. Feruglio¹⁵, M. Moresco¹⁴, M. Onodera^{16,17}, L. Pozzetti⁵, A. Renzini^{18,16}, M. Sargent¹⁹, F. Valentino², and A. Zanella²

¹ School of Physics, Korea Institute for Advanced Study, Hoegiro 85, Dongdaemun-gu, 02455 Seoul, Republic of Korea
e-mail: rgobat@kias.re.kr

² Laboratoire AIM-Paris-Saclay, CEA/DSM-CNRS-Université Paris Diderot, Irfu/Service d'Astrophysique, CEA Saclay, Orme des Merisiers, 91191 Gif-sur-Yvette, France

³ Department of Physics, Ludwig-Maximilians-Universität, Scheinerstr. 1, 81679 München, Germany

⁴ INAF-IASF, via Bassini 15, 20133 Milano, Italy

⁵ INAF-Osservatorio Astronomico di Bologna, via Ranzani 1, 40127 Bologna, Italy

⁶ Department of Astronomy, University of Science and Technology of China, Hefei, 230026, PR China

⁷ Key Laboratory of Modern Astronomy and Astrophysics in Ministry of Education, School of Astronomy and Space Science, Nanjing University, 210093 Nanjing, PR China

⁸ Institute of Cosmology and Gravitation, Dennis Sciama Building, Burnaby Road, Portsmouth PO1 3FX, UK

⁹ Dark Cosmology Centre, Niels Bohr Institute, University of Copenhagen, Juliane Mariesvej 30, 2100 Copenhagen, Denmark

¹⁰ Institute for Astronomy, Astrophysics, Space Applications and Remote Sensing, National Observatory of Athens, 15236 Athens, Greece

¹¹ European Southern Observatory, Karl-Schwarzschild-Strasse 2, 85748 Garching, Germany

¹² Department of Physics, University of Oxford, Keble Road, Oxford OX1 3RH, UK

¹³ Institute for Astronomy, ETH Zurich, 8093 Zurich, Switzerland

¹⁴ Department of Physics and Astronomy, University of Bologna, Viale Berti Pichat 6/2, 30127 Bologna, Italy

¹⁵ INAF-Osservatorio Astronomico di Trieste, via G.B. Tiepolo 11, 34143 Trieste, Italy

¹⁶ Subaru Telescope, National Astronomical Observatory of Japan, National Institutes of Natural Sciences (NINS), 650 North A'ohoku Place, Hilo, HI 96720, USA

¹⁷ Department of Astronomical Science, SOKENDAI (The Graduate University for Advanced Studies), 650 North A'ohoku Place, Hilo, HI 96720, USA

¹⁸ INAF-Osservatorio Astronomico di Padova, Vicolo dell'Osservatorio 5, 35122 Padova, Italy

¹⁹ Astronomy Centre, Department of Physics and Astronomy, University of Sussex, Brighton, BN1 9QH, UK

Received 5 October 2016 / Accepted 20 December 2016

ABSTRACT

We present a sample of 34 spectroscopically confirmed BzK -selected $\sim 10^{11} M_{\odot}$ quiescent galaxies (pBzK) in the COSMOS field. The targets were initially observed with VIMOS on the VLT to facilitate the calibration of the photometric redshifts of massive galaxies at $z \gtrsim 1.5$. Here we describe the reduction and analysis of the data, and the spectrophotometric properties of these pBzK galaxies. In particular, using a spatially resolved median 2D spectrum, we find that the fraction of stellar populations with ages < 1 Gyr is at least 3 times higher in the outer regions of the pBzK galaxies than in their cores. This results in a mild age gradient of $\Delta \text{age} \leq 0.4$ Gyr over ~ 6 kpc and suggests either the occurrence of widespread rejuvenation episodes or that inside-out quenching played a role in the passivation of this galaxy population. We also report on low-level star formation rates derived from the [OII]3727 Å emission line, with $SFR_{\text{OII}} \sim 3.7\text{--}4.5 M_{\odot} \text{ yr}^{-1}$. This estimate is confirmed by an independent measurement on a separate sample of similarly-selected quiescent galaxies in the COSMOS field, using stacked far-infrared data ($SFR_{\text{FIR}} \sim 2\text{--}4 M_{\odot} \text{ yr}^{-1}$). This second, photometric sample also displays significant excess at 1.4 GHz, suggestive of the presence of radio-mode AGN activity.

Key words. galaxies: high-redshift – galaxies: elliptical and lenticular, cD – galaxies: formation – galaxies: stellar content – galaxies: star formation

1. Introduction

Since the passing of the cosmic high noon and the peak of star formation in the Universe, the most massive galaxies have been largely quiescent, with low to undetectable

rates of star formation and so-called early-type morphologies. Their evolution since $z \sim 1$ has been traced and extensively investigated for well over a decade (e.g., Kauffmann et al. 2004; Thomas et al. 2005; Gallazzi et al. 2006). At higher redshift, and especially above $z \sim 1.5$, quiescent galaxies form a conspicuous minority population (e.g., Cimatti et al. 2004; McCarthy et al. 2004; Daddi et al. 2005), now often used as a tracer of overdense structure (Gobat et al. 2011; Spitler et al. 2012; Chiang et al. 2014; Strazzullo et al. 2015).

* The stacked VIMOS spectrum of all A+B quality ETGs is only available at the CDS via anonymous ftp to cdsarc.u-strasbg.fr (130.79.128.5) or via <http://cdsarc.u-strasbg.fr/viz-bin/qcat?J/A+A/599/A95>

They have so far been spectroscopically confirmed up to $z \sim 3$ (van Dokkum et al. 2008; Gobat et al. 2012; Hill et al. 2016), with adequate (≥ 10) samples now existing up to $z \sim 2$ (e.g., Tanaka et al. 2013; Whitaker et al. 2013; Gobat et al. 2013; Belli et al. 2014; Newman et al. 2014; Krogager et al. 2014). Their appearance only ~ 2 Gyr after the Big Bang, as well as their ages and abundances at $z > 1.5$, imply that their progenitors must have converted their gas into stars on short timescales and that the suppression of star formation happened relatively rapidly (Onodera et al. 2015). Furthermore, observational data at both low and high redshift suggest that the timescale for the quenching of star formation in massive ($\geq 10^{11} M_{\odot}$) galaxies does not depend on the local environment but is mostly set by processes internal to their host halo (e.g., Baldry et al. 2006; Thomas et al. 2010; Peng et al. 2010; Gobat et al. 2013; Newman et al. 2014). This so-called “mass quenching” can in principle be mediated by a variety of unrelated mechanisms, such as: virial shock heating of infalling gas in $> 10^{12} M_{\odot}$ halos (Birnboim & Dekel 2003; Dekel & Birnboim 2006, commonly referred to as halo quenching), stabilization of gas through bulge growth (or inside-out, sometimes also called morphological, quenching; Martig et al. 2009), and various feedback processes from either the central nucleus (e.g., Granato et al. 2004; Di Matteo et al. 2005; Croton et al. 2006; Hopkins et al. 2006) or star formation (e.g., Ceverino & Klypin 2009; Feldmann & Mayer 2015) which can directly expel the gas from the galaxies or contribute to the heating of halo gas. However, whether one of these candidate mechanisms is truly dominant during the initial quenching, or whether the suppression of star formation in massive galaxies requires a combination of factors (e.g., Woo et al. 2015), is still not well understood.

On the other hand, these various quenching processes differ in their timescales and some mechanisms (radio-mode AGN feedback, virial shock heating) are expected to leave in quenched galaxies a substantial amount of gas (e.g., Gabor et al. 2010) that can sustain some star formation activity long after the initial quenching event. While the direct detection of gas reservoirs in high-redshift quiescent galaxies remains on the edge of instrumental feasibility (Sargent et al. 2015), constraints on recent and ongoing star formation can be obtained from other indicators. For example, clues on the star formation history (SFH) prior to quenching can be derived from optical spectroscopy, although such analysis requires a good signal-to-noise ratio (S/N) and is therefore usually performed on $z < 1$ galaxies (e.g., Choi et al. 2014; Gallazzi et al. 2014; Shetti & Cappellari 2015; Citro et al. 2016). At higher redshifts, composite near-infrared (NIR) spectra are typically needed (e.g., Onodera et al. 2012, 2015; Whitaker et al. 2013; Lonoce et al. 2014). When these are not available, rest-frame ultraviolet (UV) light can function as a loose proxy of recent star formation (e.g., Rettura et al. 2010, 2011), while more recently deep mid-infrared (MIR) and far-infrared (FIR) observations have been used to estimate the residual star formation rate (SFR) of the massive $z > 1$ quiescent population (Wagner et al. 2015; Man et al. 2016). On the other hand, this latter approach is limited by the fact that neither the UV or IR indicators used are uniquely correlated with ongoing star formation, but can also originate from old stellar populations (e.g., Fumagalli et al. 2014), which makes the results of a purely photometric analysis ambiguous.

In this paper, we present an analysis of spectroscopic observations of a sample of massive, *BzK*-selected quiescent galaxies in the COSMOS field (Scoville et al. 2007). These were originally obtained to help optimize photometric redshifts for $z \gtrsim 1.5$ passive galaxies, and a comparison of spectroscopic and

photometric redshifts for this sample has already been presented in Strazzullo et al. (2015). Furthermore, an analysis of their spectral energy distributions (SED) is described in Capozzi et al. (2016). Here we report on stellar populations properties and star formation rates from both spectroscopic and FIR tracers. This paper is structured as follows: in Sect. 2 we present the sample, the observations, and describe the method used to derive spectroscopic redshifts; we detail our spectroscopic analysis in Sects. 3 and 4; we discuss its implications in Sect. 5, and summarize our conclusions in Sect. 6. A table with the spectroscopic redshifts of this sample is given in Appendix A. We assume a Λ CDM cosmology with $H_0 = 70 \text{ km s}^{-1} \text{ Mpc}^{-1}$, $\Omega_M = 0.27$, and $\Omega_{\Lambda} = 0.73$, and all cited quantities assume a Salpeter (1955) initial mass function (IMF).

2. Sample selection and data reduction

We selected galaxies from the catalog of McCracken et al. (2010), identified as passive using the *BzK* criterion (Daddi et al. 2004), and brighter than $I_{AB} = 25$, so as to be detectable in at most a few nights of spectroscopic observations at optical/NIR wavelengths. This criterion yielded ~ 2700 passive *BzK* (*pBzK*) galaxies over the full COSMOS field, from which we selected an area containing 78 *pBzKs*. Among these galaxies, we targeted 29 *pBzKs* that were undetected at $24 \mu\text{m}$ in the 2010 catalog. The configuration of the spectroscopic mask allowing it, we included another 6 *pBzKs* that were detected in *Spitzer*/MIPS imaging, for a total of 35 targets. This corresponds to 56% of *pBzKs* with $\log M_{\star} > 10.8$ in the target area, and 90% of those with $\log M_{\star} > 11.3$. These galaxies were observed with VIMOS on the VLT in service mode, during ESO programs 086.A-0681 and 088.A-0671 (February-March 2011 and February-March 2012, respectively; PI E. Daddi). The total exposure time per field was 10.5 h, split into 72 exposures of 523 s each. We used the medium resolution grism, with a dispersion of 2.5 \AA per pixel ($0.205''$ in the spatial direction), coupled to the GG475 order-sorting filter which limits the wavelength range to 4500–10000 \AA , and a slit width of $1''$ corresponding to a resolution of $R = 580$. To allow for better background subtraction, we applied the “nod along slit” technique, with a shift of $2''$ between one exposure and another, for a total of 5 positions. The airmass during the observation was ~ 1.15 , while the typical seeing was better than $1''$. The data were then reduced using the VIPGI pipeline (Scodreggio et al. 2005) as follows: the position of each 2D spectrum was first determined for each single exposure using the flat field; sky subtraction was then performed on the bias-subtracted raw data by fitting a 1D polynomial in each wavelength bin; the spectra were then extracted and calibrated in wavelength by applying the inverse dispersion solution (IDS). To account for instrument flexure, the IDS was derived from an arc line exposure taken immediately prior to or following the scientific one. A second background subtraction pass was then performed on the extracted 2D spectra, using a background map for each slit constructed by combining individual frames without applying any offset. Frames were then offset according to the observing sequence and combined. Each 1D spectrum was then extracted using optimal extraction and corrected for the instrument’s sensitivity, with a sensitivity curve obtained from observations of a red star. As the observations were performed during several nights in different meteorological conditions, the resulting spectra are in (arbitrary) pseudo-flux units.

Redshifts. We derive redshifts for 34 of the 35 extracted *pBzK* spectra. The distribution of spectroscopic redshifts, which has a median of $z = 1.51$, is shown in Fig. 1 and the full list given

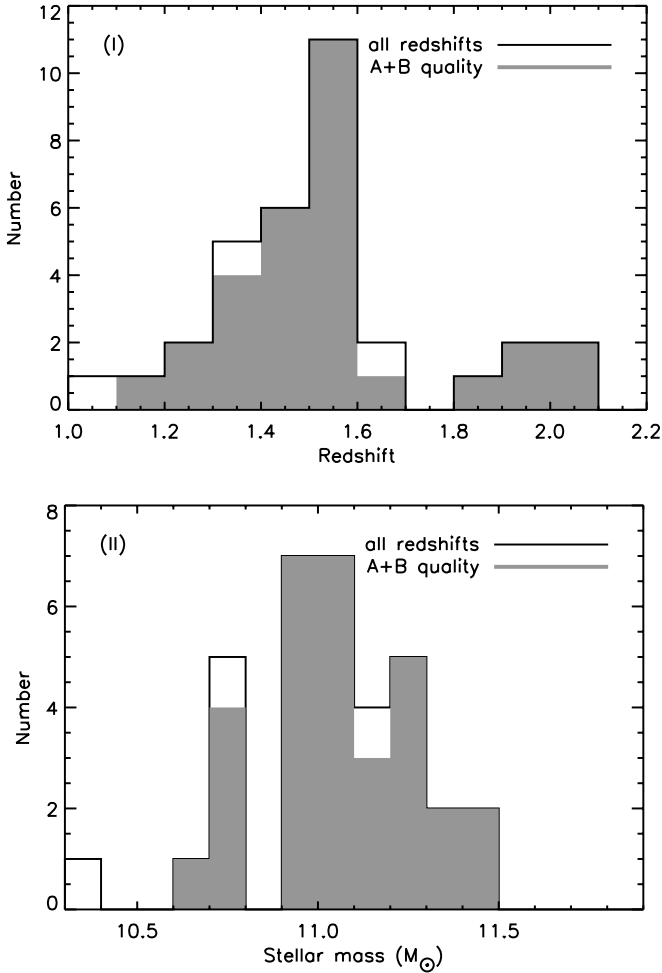


Fig. 1. *Top:* distribution of spectroscopic redshifts (solid histogram) derived from fitting the observed spectra with stellar population models, with the shaded histogram showing the secure ones. *Bottom:* distribution of stellar masses (Salpeter IMF) derived from UltraVISTA photometry, using the same grid of models.

in Appendix A. We estimate redshifts with two different methods: (i) by measuring absorption lines using the *rvidlines* IRAF task and estimating uncertainties from the rms of centroid positions; or (ii) through fitting of the full spectra with templates. For the latter method we use either average spectra from the K20 and GMASS surveys (Cimatti et al. 2002; Kurk et al. 2013) or a grid of stellar population models based on Bruzual & Charlot (2003, BC03) single stellar population (SSP) templates. In this case we assume a delayed, exponentially declining SFH, with ages between 0.1 and $\min(t_z, 6)$ Gyr (where t_z is the age of the Universe at redshift z) and characteristic timescale values between 1 Myr and 2 Gyr. We fit each composite model (continuum+lines) individually and estimate the confidence interval on the redshift from the χ^2 distribution, using for each object the noise spectrum produced by the pipeline as error spectrum. We include the effect of dust extinction, following the Calzetti et al. (2000) prescription with $E(B - V) = 0-1$. We adopt a regularly spaced redshift grid with an initial coarse step of $\Delta z = 0.001$, which we refine to $\Delta z = 10^{-4}$ once a solution has been identified. Because the S/N of the spectra is generally low (~ 1 per pixel), this method tends to be more efficient at estimating redshifts than simply correlating the positions of (apparent) absorption lines. Examples of full-spectrum fits are shown in Fig. 2. We assign

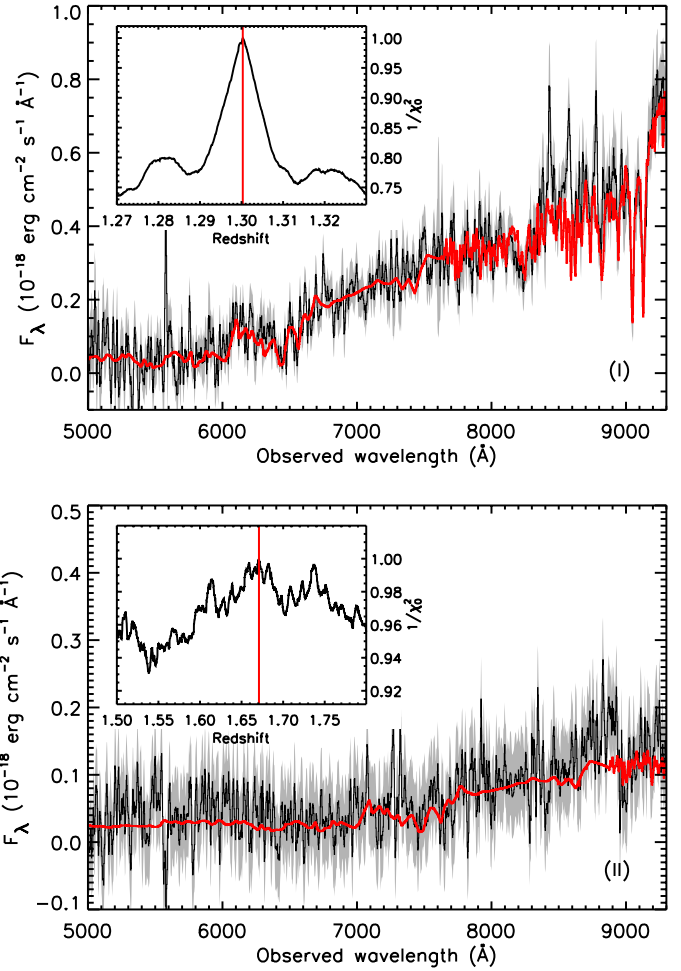


Fig. 2. Examples of a secure (*top*; “A” quality; ID 225039) and an uncertain (*bottom*; “C” quality; ID 240680) redshift. In each case, the black curve shows the observed spectrum, with error in gray, and the red one the best-fit model. The *inset* shows the inverse of the reduced χ^2 , with the best-fit solution marked by a red vertical line. Each spectrum has been rebinned to a width of 5 pixels.

to the resulting redshifts a quality flag based on the following criterion: spectra for which the fit has a unique solution and the two methods yield consistent estimates are given the quality flag “A”; on the other hand, we use the quality flag “B” for spectra for which the first method fails (i.e., no clear absorption features can be seen in the spectrum) but the template fit still yields a single strong solution; finally, we assign quality flag “C” to spectra for which the fit has one or more secondary solutions and no redshift can be estimated by other methods. Redshifts of A or B quality are considered secure, while C quality redshifts are uncertain. Uncertainties on the redshifts are estimated from the χ^2 of the template fit, after rescaling so that it be 1 per degree of freedom if originally higher. The redshift uncertainties thus derived have a median value of $\sigma_z = 0.0009$. We obtain 20 A, 11 B, and 3 C quality redshifts, respectively, with only one spectrum in the sample having too low S/N for either method to yield a meaningful estimate. Considering only the secure redshifts, this corresponds to a success rate of 89% for the spectroscopically detected objects and a completeness of 40% when including all pBzK galaxies in the target area.

We match the positions of the spectroscopically confirmed pBzKs to the multiband catalog of Muzzin et al. (2013), which

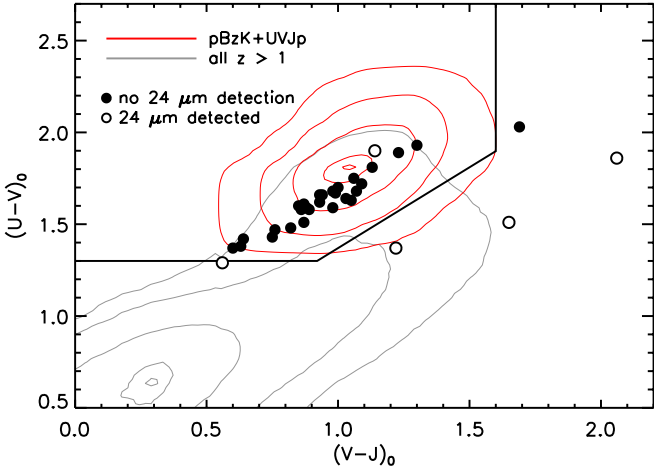


Fig. 3. Rest-frame $U - V$ vs. $V - J$ diagram of galaxies in the COSMOS field. Filled circles mark the position of our pBzK galaxy sample in color-color space, with empty ones indicating $24 \mu\text{m}$ detections. The red and gray contours show, respectively, the distribution of $BzK + UVJ$ -selected quiescent galaxies (see Sect. 4.2) and $z > 1$ galaxies, using the same relative scale.

is based on the UltraVISTA survey of the COSMOS field (McCracken et al. 2012). Ignoring the GALEX bands due to their lower resolution, we model the remaining 28-band photometry with the same grid of stellar population models as described above (fixing the redshift but letting the other parameters vary) to estimate stellar masses and dust extinction values. The distribution of these stellar masses, which has a median of $M_{\star} = 1.1 \times 10^{11} M_{\odot}$, is shown in Fig. 1. We note that it is consistent with the BC03 masses given in Capozzi et al. (2016), although the values for individual galaxies differ owing to differences in the SFH and parameter grid used. As a sanity check, we also use the best-fit models to the SED to compute rest-frame $U - V$ and $V - J$ colors and confirm that most of the pBzK galaxies are selected as passive using the high-redshift UVJ criterion of Williams et al. (2009), except for the $24 \mu\text{m}$ ones. As shown in Fig. 3, the former are well within the locus of $z > 1$ quiescent galaxies.

3. Stellar population properties

Next, we create a median 2D spectrum of the spectroscopically confirmed A and B quality pBzKs, shifting each reduced 2D spectrum to the median redshift of $z = 1.51$ and correcting for cosmological dimming. We then shift the 2D spectra in the spatial direction so that the peak of the spectral trace falls onto the central pixel. For each source, we estimate the y position of the trace by fitting a simple Gaussian peak to its median profile along the dispersion direction. We find that the rms offset of individual spectra in the spatial direction is ≤ 0.3 pixel. Individual spectra are then here weighted by their intrinsic rest-frame UV-optical luminosity. We also compute a 2D variance spectrum, where the value of each pixel corresponds to the median absolute deviation of fluxes at each pixel position in the stack. We note that the typical redshift uncertainty corresponds to $< 50\%$ of the spectral resolution, and that it thus has negligible impact on the stack. The resulting 1D spectrum, extracted over the entire cross-dispersion column, is shown in Fig. 4 and will be made available as an ASCII table at the CDS (the file contains the following information: Col. 1 gives the rest-frame wavelength in

\AA , while Cols. 2 and 3 give, respectively, the flux and flux uncertainty estimated from the variance spectrum, both in arbitrary f_{λ} units). We characterize this spectrum using SSP templates from Maraston & Strömbäck (2011, hereafter M11), with resolution matched to that of our VIMOS spectra. These templates are based on the MILES stellar library (Sánchez-Blázquez et al. 2006) but have been extended to the far UV and thus cover the whole rest-frame wavelength range spanned by the stacked spectrum. They have ages between 0.1 and 4 Gyr and four different metallicities of 2% to twice the solar value. We estimate uncertainties on derived parameters from the 68% confidence intervals of the χ^2 fit. We note that flux errors derived from the variance spectrum are a factor ~ 10 higher than the rms noise in the background regions of the 2D median spectrum, yielding conservative uncertainty estimates on the derived parameters. We find a luminosity-weighted age of $1.5^{+1.5}_{-0.5}$ Gyr, and use the high-S/N rest-frame UV absorption features (Mg II, Mg I, NH 3360, and BL 3580; Fanelli et al. 1990; Davidge & Clark 1994; Serven et al. 2011) to constrain the luminosity-weighted metallicity at $1^{+0.6}_{-0.2} Z_{\odot}$. These values are consistent with the range of derived ages and metallicities in massive quiescent galaxies at this redshift, from either rest-frame UV or rest-frame optical spectra (Cimatti et al. 2004; McCarthy et al. 2004; Daddi et al. 2005; Onodera et al. 2015).

This median spectrum also displays two other noteworthy features: First, it shows clear [OII]3727 \AA line emission. Second, it is marginally resolved, as its profile in the cross-dispersion (spatial) direction is more extended than the stacked spectrum of 3 stars taken during the same observation (Figs. 5 and 8). To investigate this further, we redo the stack considering only the pBzKs with redshift below the median ($z < 1.5$), i.e., whose spectrum is not truncated before the 4000 \AA break, since it is the region with the most useful features for stellar population modeling. This also has the advantage that the resulting subsample covers ~ 1 Gyr of cosmic time and thus a relatively narrow epoch in the galaxies' evolution. We also remove possible AGNs from the stack by selecting only sources which are not detected in *Spitzer*/MIPS $24 \mu\text{m}$ data and not classified as AGNs either in the photometric catalog or with the updated IRAC color criterion of Donley et al. (2012). This criterion yields 13 sources with a median redshift of $z = 1.4$ and a median stellar mass of $M_{\star} = 1.1 \times 10^{11} M_{\odot}$, identical to that of the parent sample. A portion of the resulting median stack is shown in Fig. 5. We estimate uncertainties for each pixel using bootstrap resamplings of the data, with sizes of half the initial sample.

3.1. Spatial decomposition and spectral extraction

We then extract 1D spectra from the 2D composite spectrum in three different apertures: an inner 3-pixel one centered on the peak of the cross-dispersion profile, an outer aperture extending 5 pixels on each side of the central aperture (Fig. 5), and a full (inner + outer) one. These widths were chosen so that the inner and outer extracted spectra are mostly independent from each other, the width of the inner aperture being comparable to the FWHM of the stellar stack (3.5 pixels), while also minimizing differences in S/N between the two spectra. As shown in Fig. 7, they are broadly similar except around 4000 \AA , where the outer aperture spectrum appears to have a shallower 4000 \AA break (we note however that there is not enough continuum redward of the break to compute a spectral index) and a deeper 3969 \AA line than the inner one, suggesting excess He absorption and thus more recent star formation.

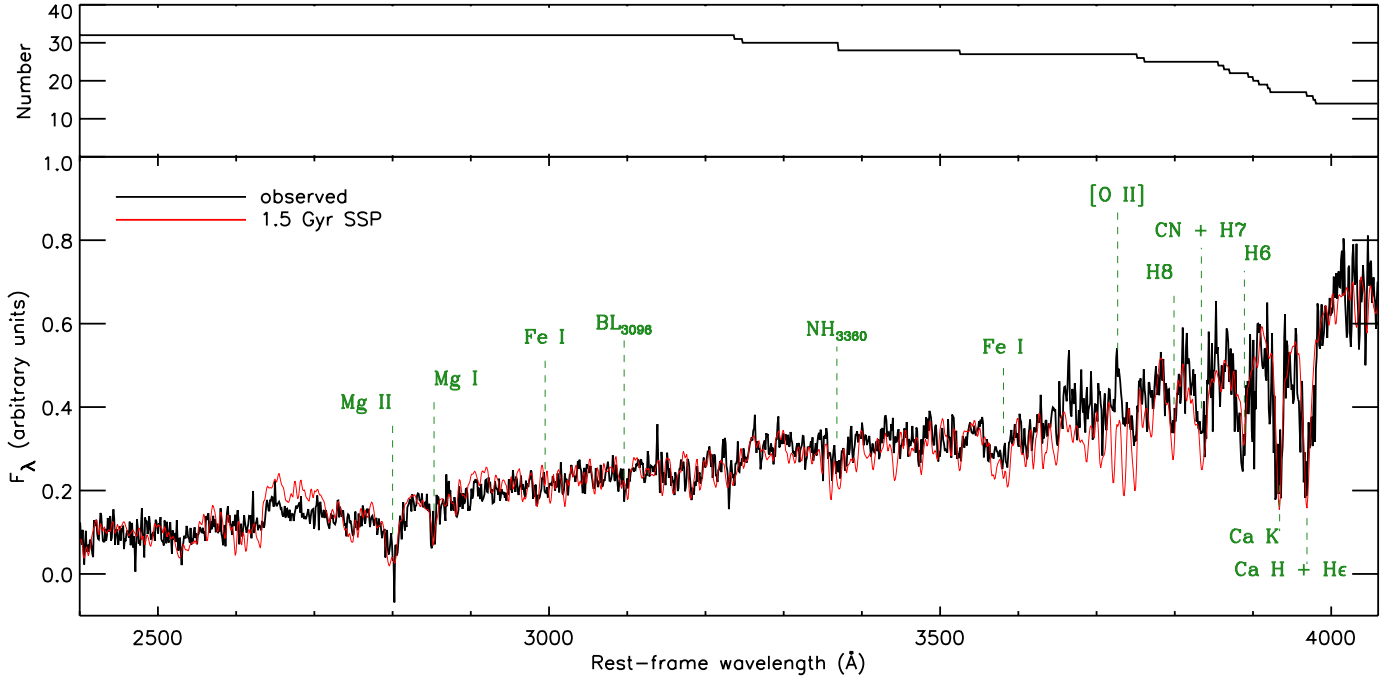


Fig. 4. *Top:* number of A and B quality spectra contributing to the median spectrum as a function of rest-frame wavelength. *Bottom:* stack of all A and B quality spectra, as a function of rest-frame wavelength, with a 1.5 Gyr SSP template (Maraston & Strömbäck 2011) for comparison. Prominent spectral features are indicated in green.

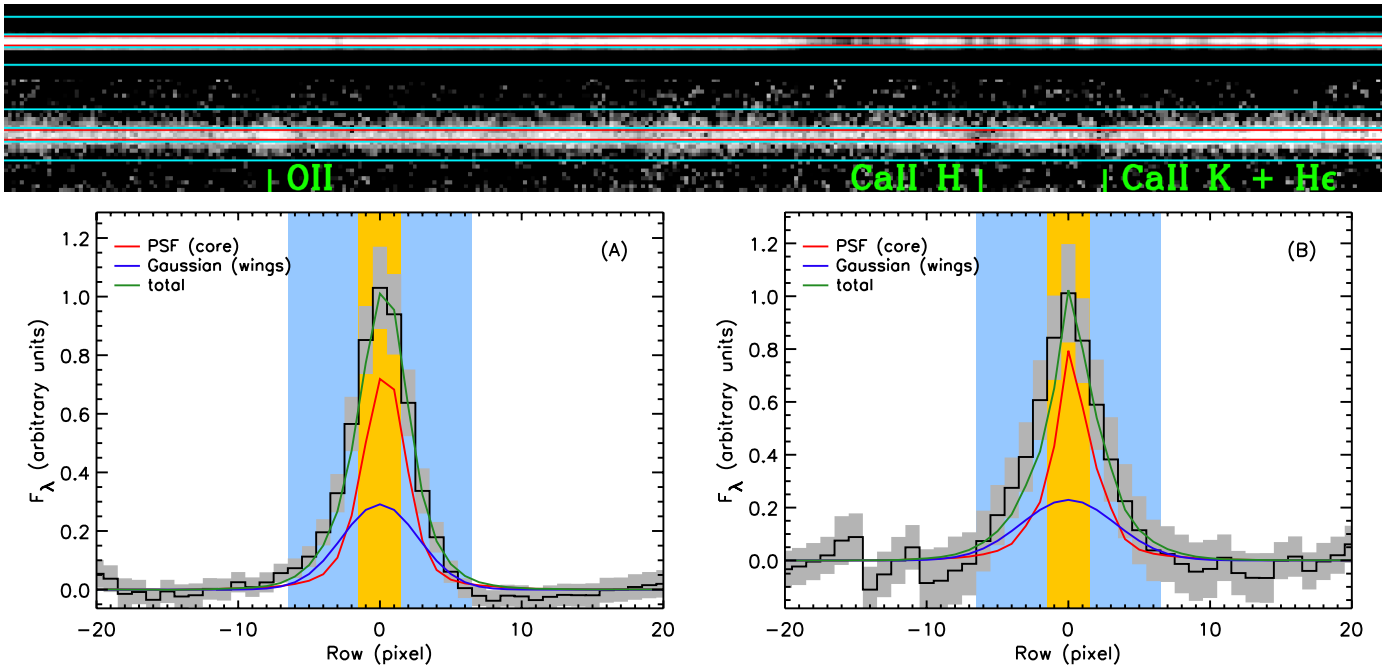


Fig. 5. *Top:* median 2D spectra of stars (top row) and pBzKs in the range $z = 1.2$ – 1.5 (bottom row), in the same wavelength range and using the same relative flux scale. Prominent features in the stacked galaxy spectrum are indicated in green. The red and cyan lines show the inner and outer extraction apertures, respectively. *Bottom:* cross-dispersion profile of the stacked pBzK spectrum at 3650–4050 Å rest-frame (dark histogram with gray errors), fit with a combination of a point-source (red) and a Gaussian (blue) profile. The inner and outer extraction apertures are indicated by the orange and light blue shaded regions, respectively. Panels **A**) and **B**) show, respectively, the cross-dispersion profiles before and after correcting for galaxy morphology. Only the profile shown in panel **A**) was used for the decomposition and analysis described in Sect. 3.1 and below.

This apparent stellar population difference could be due to our including in the stack populations of galaxies quenched at different epochs, with the younger ones being also larger and thus contributing more to the flux in the outer aperture (see, e.g., Carollo et al. 2013; Williams et al. 2017). To test this we look at the publicly available HST/ACS *F814W* mosaic

(Koekemoer et al. 2007), corresponding here to the rest-frame 3300–3700 Å. We measure the ratio of *F814W* flux in two apertures of diameter equal to the spectroscopic ones (a measure of compactness in the rest-frame UV) and compare it to the rest-frame $U - B$ color of the galaxies (which measures the amplitude of the 4000 Å break). Only 14 out of 34 spectroscopically

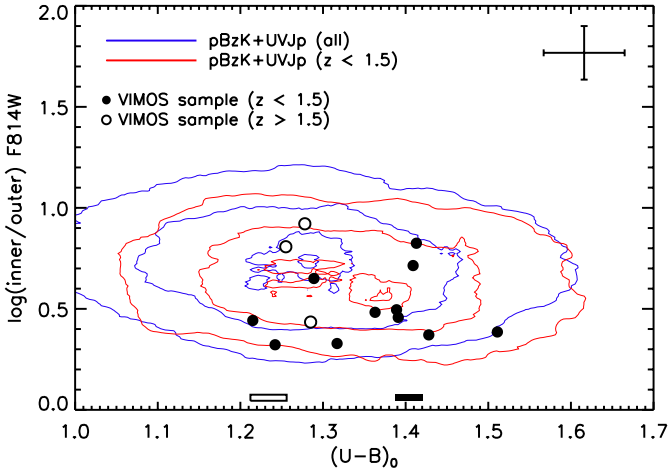


Fig. 6. Ratio of rest-frame UV flux in the inner and outer aperture, based on the HST/ACS *F814W* mosaic, as a function of rest-frame $U-B$ color. Filled and empty circles show pBzKs below and above $z = 1.5$, respectively, using the same relative scale. The blue and red contours mark the distribution of $BzK + UVJ$ -selected galaxies (see Sect. 4.2) in the full $z = 1.5-2.5$ range and at $z < 1.5$, respectively. The error bars in the upper right corner show the typical uncertainty on both quantities while the filled and empty bars show the rest-frame color distribution of low-S/N pBzKs at $z < 1.5$ and $z > 1.5$, respectively.

galaxies have high enough S/N in the *F814W* image to allow for such a comparison. Since we only consider galaxies with high enough surface brightness, this could effectively be assimilated to a selection in age. However, the rest-frame colors of low-S/N pBzKs are consistent with those of the higher-S/N galaxies. We perform this test for both these 14 pBzKs and a sample of all BzK - and UVJ -selected galaxies in the COSMOS field (see Sect. 4.2 for details on this second selection). As shown in Fig. 6, we find no correlation between the ratio of *F814W* light in the inner to outer aperture, measured using the circularized profile of the detected pBzKs, and their rest-frame $U-B$ color estimated from the SED fit. This suggests that compactness in the rest-frame UV is not strongly correlated with the combination of age and metallicity traced by the color. Both the color and compactness of our pBzKs also appear to be consistent with the distribution of the larger sample. While we see no evidence for a correlation between the global stellar populations of our galaxies and their compactness, the combination of differently-sized objects can still have an effect on derived properties in the inner and outer apertures. Assuming that all galaxies in our sample have similar stellar population structure, we estimate from Fig. 6 that their combination in the stack should make us underestimate stellar population differences between the two apertures by $\sim 10\%$. This is however well within the uncertainties we derive below.

If we then assume that the stellar populations of the pBzKs can be spatially separated into two components, one compact and central (“core”) and the other extended (“wings”), the intrinsic spectra of the core and wings components (f_c and f_w , respectively) are related to the observed spectra in the inner and outer apertures (f_i and f_o , respectively) as follows:

$$\begin{pmatrix} f_i \\ f_o \end{pmatrix} = \begin{pmatrix} w_{ic} & w_{iw} \\ w_{oc} & w_{ow} \end{pmatrix} \begin{pmatrix} f_c \\ f_w \end{pmatrix} + \begin{pmatrix} \delta f_i \\ \delta f_o \end{pmatrix}, \quad (1)$$

where δf is the noise per pixel column in each aperture and the mixing parameters w are the fraction of light in either aperture coming from the core and wings spectra. We consider

two different decompositions of the spectrum: in the first, we parameterize the cross-dispersion profile of the stacked pBzK spectrum as a combination of a point source (for the core) and a Gaussian (for the wings), as shown in Fig. 5. We use the profile from a 2D stack of 3 stellar spectra for the point source and perform the decomposition on the median profile stacked along the dispersion direction; under these assumptions, $[w_{ic}, w_{iw}, w_{oc}, w_{ow}] = [0.76, 0.24, 0.48, 0.52]$, with uncertainties of $[0.03, 0.03, 0.02, 0.02]$ (we note that these contribute negligibly to the error spectrum, compared to the pixel variance). The resulting core and wings spectra are shown in Fig. 7. For the second, based on the observed i -band morphologies of massive early-type galaxies (ETGs) in the COSMOS field (Mancini et al. 2010), we assume that the tridimensional distribution of stars in the pBzK galaxies can be described by a deprojected de Vaucouleurs density profile (Mellier & Mathez 1987). We then define the core (respectively, wings) as the light within (outside) 4.6 kpc, the effective radius estimated from fitting a 1D de Vaucouleurs profile to the observed cross-dispersion profile (we note that this value is consistent with the ACS sample of Mancini et al. 2010). We reproject and convolve these two fractional profiles with the stellar point spread function to find their respective contributions to the inner and outer apertures. This yields $[w_{ic}, w_{iw}, w_{oc}, w_{ow}] = [0.61, 0.39, 0.44, 0.56] \pm [0.002, 0.002, 0.001, 0.001]$ and 1D spectra similar to the ones obtained with the first parameterization.

We then perform a series of tests to check the robustness of our profile decomposition. First, we shift the median spectrum by ± 0.5 pixel in the spatial direction, to conservatively simulate the uncertainty in the trace position. We find that this changes the mixing parameters by 0.01 for the core and 0.015 for the wings. Next, to probe the effect of combining differently-sized sources on the median profile, we construct a 2D median spectrum where the individual cutouts have been corrected for galaxy sizes. We rescale the 2D spectra of galaxies detected in the *F814W* mosaic by the ratio of their size in the slit (estimated from their circularized effective radius, axis ratio, and position angle) to the median value, while leaving those of undetected sources untouched. The expanded or contracted 2D spectra are then drizzled back onto the original grid, assuming empty pixels for missing data. Since this effectively modifies the spatial resolution of the spectrum, we repeat this operation using, for each galaxy, the 2D stellar spectrum to derive a modified point source profile. This increases w_{ic} and decreases w_{iw} by 0.1. On the other hand, the size-corrected 2D spectrum samples the stacked profile less well, as objects larger than the median are rebinned to a coarser pixel grid. This procedure also yields higher and more correlated per-pixel noise, resulting in higher flux uncertainties on the extracted 1D spectra. Consequently, quantities derived from the analysis presented in Sect. 3.2 become unconstrained when using the size-corrected spectra, although they appear to follow the same trends. Finally, we note that all these different mixing parameters yield extracted core and wing spectra that are consistent with each other within uncertainties.

3.2. Spectral modeling

We model the extracted spectra with linear combinations of high-resolution SSP templates. In addition to the aforementioned M11 models, we also consider those of Vazdekis et al. (2010, hereafter V10), also based on the MILES library but computed with different stellar evolution prescriptions. They also cover a larger metallicity range, with $\log(Z/Z_\odot) = -2.32$ to 0.22, but are

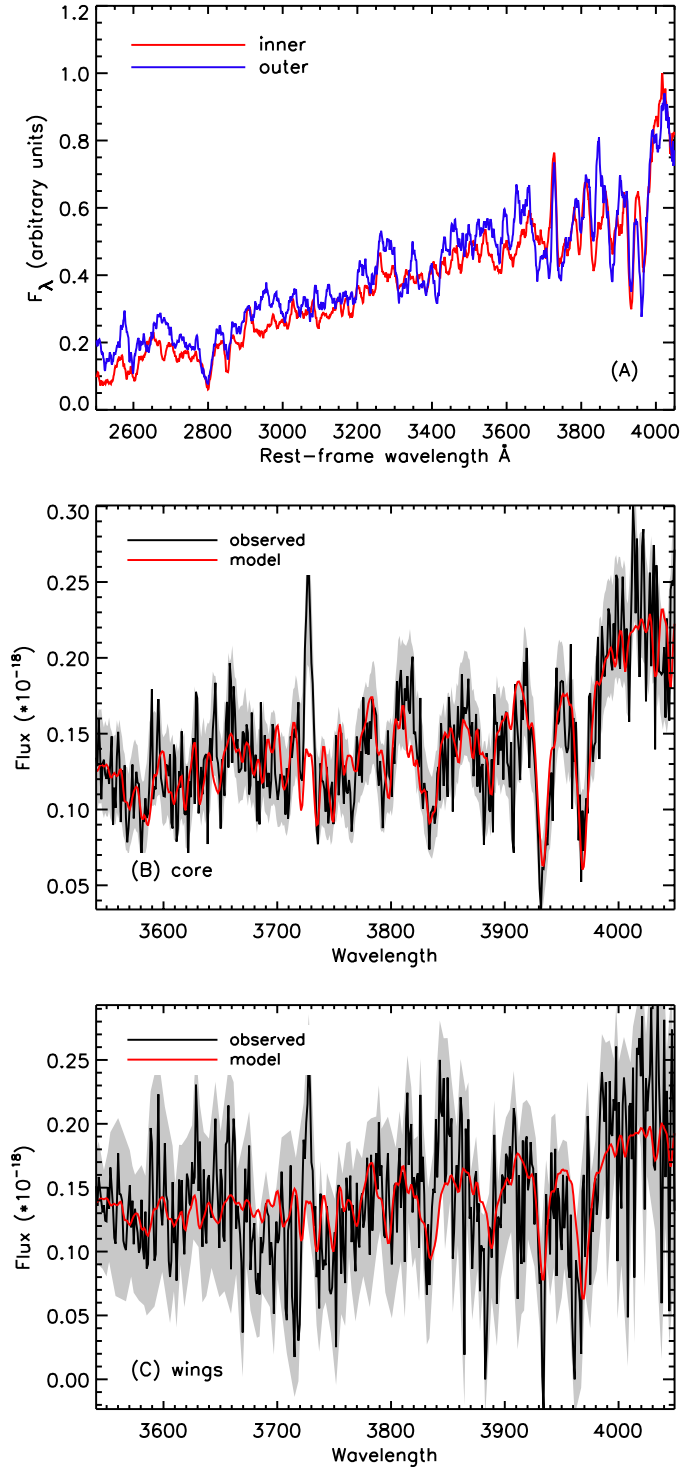


Fig. 7. **A)**: extracted inner (red) and outer (blue) spectra rebinned to a 10 pixel width. **B)** and **C)**: unrebinned core and wings spectra, respectively, decomposed according to Eq. (1) (black), with associated uncertainties (gray) and best-fit combination of SSP templates (red).

only defined down to 3540 Å. As previously stated, we consider ages between 0.1 and 4 Gyr. We convolve the templates with a fixed Gaussian to match the resolution of the spectra and fit for the templates weights with MPFIT (Markwardt 2009), using bounds to enforce nonnegativity. We do not attempt to fit the kinematics of this sample since the spectral resolution, which at this redshift corresponds to $\gtrsim 200 \text{ km s}^{-1}$, is of the order of

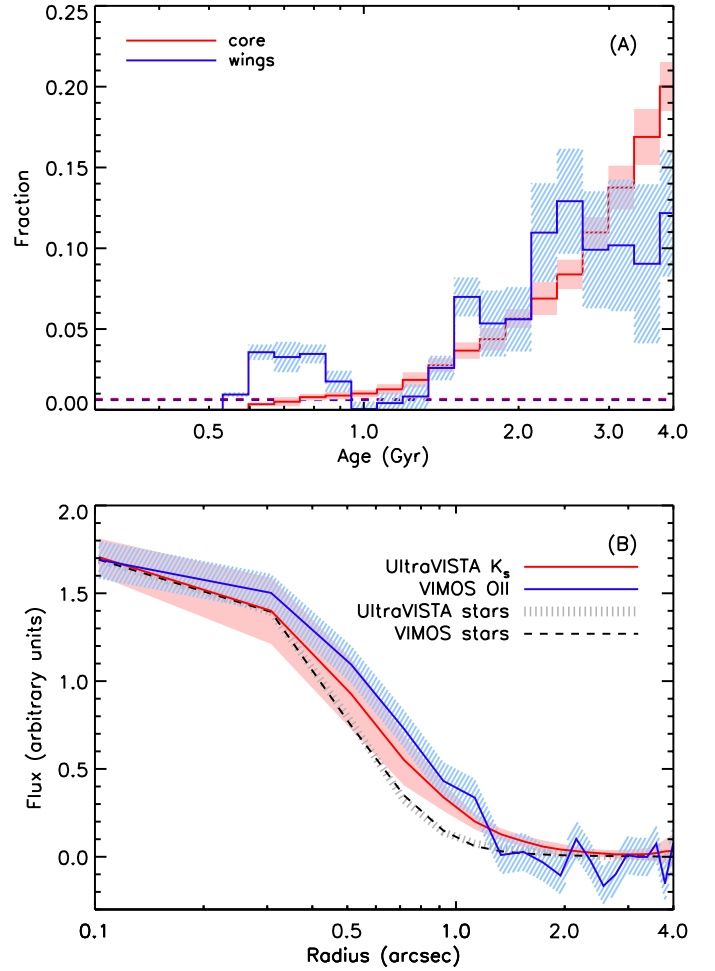


Fig. 8. **A)**: relative weight as a function of age of V10 SSP templates in the fit to the core and wings spectra (red and blue, respectively). The horizontal dashed lines show the level of the SFR derived in Sect. 4.1, if we assume that the red and blue histograms represent the SFH of the core and wings, respectively. **B)**: radial profiles of the [OII]3727 Å line from the stacked VIMOS spectrum (blue) and K_s -band light (red) from UltraVISTA imaging, for the same galaxies. Both profiles are shown in 0.205'' bins and have been normalized to the same flux. The dashed and dotted curves show the profile of stars in our VIMOS spectra and the K_s -band image, respectively.

the expected velocity dispersion. We use the 1σ errors on the template weights, rescaled so that the χ^2 is one per degree of freedom, to estimate the uncertainties on the quantities derived from the fit. We restrict ourselves to $<4050 \text{ Å}$ rest-frame, since the flux calibration becomes unreliable at redder wavelengths. We also mask the region of the spectrum corresponding to the [OII]3727 Å line. The best-fit models to the core and wings spectra are shown in Fig. 7 and the reconstituted SFH (i.e., the distribution of template weights as a function of age) for both core and wings spectra is shown in Fig. 8.

Since the core spectrum has higher S/N than the wings, we also perform a simulation to test the dependency of the difference between their best-fit solutions to the S/N. We use the best-fit model to the core spectrum, adding noise to match the S/N of the wings spectrum, and fit it to the same grid of templates. We find that the best-fit SFHs to the core and wings spectra are consistent with one another for ages >1 Gyr, but that the best-fit wings model includes a significantly higher fraction of stellar

populations with ages <1 Gyr than the best-fit core model, suggesting more protracted star formation in the galaxies' outskirts. The relative mass fractions $f_{<1}$ of such young stellar populations are $f_{<1} = 3 \pm 1\%$ ($4 \pm 1\%$) in the core and $f_{<1} = 13 \pm 1\%$ ($21 \pm 7\%$) in the wings with the V10 (M11) templates and for the Gaussian decomposition. In the case of a de Vaucouleurs profile, these values become, respectively, $f_{<1} = 3 \pm 1\%$ ($3 \pm 1\%$) in the core and $f_{<1} = 12 \pm 2\%$ ($18 \pm 6\%$) in the wings. If we consider the undecomposed total spectrum, we find that the stellar population fraction with ages <1 Gyr is $f_{<1} = 5 \pm 1\%$. This corresponds to an average SFR of $5.6 \pm 1 M_{\odot} \text{ yr}^{-1}$ over the last 1 Gyr. We note that the actual time resolution of the spectral modeling is significantly coarser than the 0.1 Gyr step we use here. Since the fit does not take the [OII]3727 Å line or the rest-frame far-UV photometry into account, it is not expected to yield very young solutions.

The presence of this additional young stellar population in the wings generates a mild age gradient, with the best-fit models to the core and wings having (mass-weighted) average ages of 2.8 (2.9) ± 0.1 Gyr and 2.4 (2.7) ± 0.3 Gyr for the V10 (M11) templates. These values are summarized in Appendix B. As the V10 templates cover a larger metallicity range than the M11 ones, the solutions they yield tend to be smoother in age-space. Nevertheless, in both cases the >1 Gyr stellar populations have $\log(Z/Z_{\odot}) \geq -1$ while the fit yields $\log(Z/Z_{\odot}) \geq 0$ for the <1 Gyr ones, similar to the luminosity-weighted value derived from the full stack. The wavelength range of the M11 templates also allows us to model the spectrum of the $z > 1.5$ pBzKs. However, in this case, the only prominent features are the Mg II and Mg I absorption lines at 2800 Å and 2852 Å, whose behavior is both complex and subject to the well-known age-metallicity degeneracy (e.g., Fanelli et al. 1990). Furthermore, the stack of these higher redshift galaxies has lower S/N and the decomposition only yields a usable spectrum for the core (for which we find a mass-weighted age of 2 ± 1 Gyr), ruling out a comparison as described above.

4. Star formation rates

4.1. [OII]3727 Å emission

We subtract the best-fit model to the full spectrum from the observed flux and fit the residuals at 3727 Å with a (blended) double Gaussian. We thus estimate the total flux of the [OII]3727 Å line at $(3.4 \pm 0.3) \times 10^{-18} \text{ erg s}^{-1} \text{ cm}^{-2}$, with $(1.9 \pm 0.2) \times 10^{-18} \text{ erg s}^{-1} \text{ cm}^{-2}$ in the core and $(1.5 \pm 0.2) \times 10^{-18} \text{ erg s}^{-1} \text{ cm}^{-2}$ in the wings (here we only consider the core and wings spectra obtained with the Gaussian decomposition of the profile, since both parameterizations yield very similar results). This corresponds to equivalent widths (EW) of 5 ± 1 and 11 ± 2 for the core and wings, respectively. The larger EW of the [OII]3727 Å emission in the wings spectrum (this remains the case even if we compare the spectra in inner and outer aperture rather than the core and wings) implies that it is not particularly point-like but rather appears to be slightly more extended than the distribution of stellar light in the blue optical. This is not very surprising, as we have discarded AGN candidates from this subsample. We also create a stacked image using cutouts from the UltraVISTA K_s -band mosaic, centered at the position of the 13 pBzKs in the subsample. The K_s -band traces the stellar mass more than the rest-frame UV continuum, although at this redshift it can still be biased by young stellar light. Using the same stars mentioned in Sect. 3.1, we find that the K_s -band image and our VIMOS spectra have virtually identical spatial

resolution. We then compare the K_s -band surface brightness distribution of the galaxies with the cross-dispersion profile of the [OII]3727 Å line. As shown in Fig. 8, the latter appears consistent with, although slightly less concentrated than, the K_s -band profile. Likewise, the cross-dispersion profile of the stellar continuum on both sides of the [OII]3727 Å emission is indistinguishable from that of the line. We are therefore confident that the ionizing photons giving rise to the [OII]3727 Å emission seen in the stacked spectrum indeed originates from young stars (i.e., from star formation), rather than from a significant population of hot post-main sequence stars or from nuclear activity.

We correct for the loss of flux due to the narrow slit by scaling the median best-fit model to the SEDs of pBzKs to the flux of the observed spectrum in the range 3550–4050 Å. We then multiply this normalization factor by the median difference between aperture and total K_s -band magnitudes in the Muzzin et al. (2013) UltraVISTA catalog to recover the total flux. Next, we correct this [OII]3727 Å flux for dust extinction using the median value derived from the SED fit, $E(B - V) = 0.12$, assuming a Calzetti et al. (2000) extinction law and a value of $f = 0.83$ for the ratio between stellar and nebular extinction (Kashino et al. 2013, derived for $z \sim 1.55$ star-forming galaxies). We convert the [OII]3727 Å flux into a SFR using the relation of Kennicutt (1998) and find $SFR_{\text{OII}} = 4.5 \pm 1$ (3.7 ± 1) $M_{\odot} \text{ yr}^{-1}$ after (before) correcting for dust extinction. These values are consistent with the SFH inferred from the spectral modeling. Applying the same aperture-to-total correction to the stellar masses, the derived SFR corresponds to a specific SFR (sSFR) of $\sim 2.7 \times 10^{-11} \text{ yr}^{-1}$, ~ 1.6 dex below the main sequence of star formation (MS) at $z = 1.4$, assuming the parameterization of Sargent et al. (2014, hereafter S14). This is, however, 1 dex higher than the offset between local ETGs and the MS at $z \sim 0$ (Lianou et al. 2016; Man et al. 2016, hereafter M16). Using the Calzetti et al. (2000) nebular-to-continuum extinction ratio ($f = 0.44$), on the other hand, would yield $SFR_{\text{OII}} = 9 \pm 2 M_{\odot} \text{ yr}^{-1}$, or ~ 1.2 dex below the MS.

4.2. Far-infrared properties

To further probe the nature of the line emission, we turn to the far-infrared data available on the COSMOS field. We extend our spectroscopic sample by including all galaxies with photometric redshifts in the range $z = 1.2$ – 1.5 , that are selected as passive using both the BzK and UVJ criteria (hereafter pBzK+UVJp) and have $\log M_{\star} \geq 10.8$, to match the stellar mass distribution of the spectroscopic sample. We also consider a larger sample consisting of all pBzK+UVJp in the COSMOS field, with the same mass cut. We refer to the first one as the “low- z ” sample and the second as the “total” one. In both cases, we exclude objects that are individually detected at 3σ at 24 μm , using a new catalog of *Spitzer*/MIPS sources from Jin et al. (in prep.). We also ignore all possible pairs, i.e., galaxies with concordant redshifts (within $\Delta z \leq 0.2$) and separated by less than 60". This criterion yields 182 pBzK+UVJp galaxies in the low- z sample and 977 ones in total sample. Both samples have a median stellar mass of $1.2 \times 10^{11} M_{\odot}$, for a median redshift of $z = 1.44$ and $z = 1.76$, respectively. We then use MIR, FIR, and radio maps, at 24 μm (*Spitzer*/MIPS; Le Flocc'h et al. 2009), 100 and 160 μm (*Herschel*/PACS, from the PEP survey; Lutz et al. 2011), 250, 350 and 500 μm (*Herschel*/SPIRE, from the HerMES survey; Oliver et al. 2012), 850 μm (JCMT/SCUBA2; Geach et al. 2017), and 1.4 GHz (VLA; Schinnerer et al. 2010).

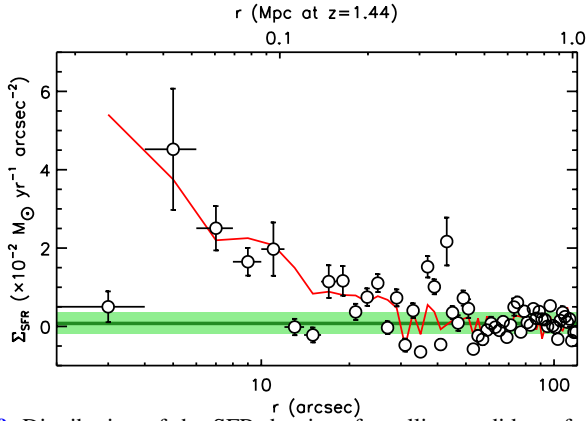


Fig. 9. Distribution of the SFR density of satellite candidates for the low- z pBzK+UVJp sample, shown in bins of $2''$ (~ 17 kpc at $z = 1.44$). The background density, estimated at $r > 50''$, is shown in green while the red curve shows, for comparison, the total number density of satellite candidates, rescaled to match the SFR profile.

For each band, we create a median 2D image from cutouts around each pBzK+UVJp galaxy 5 times larger than the beam FWHM, which we then fit with a centrally positioned point source. This procedure is similar to the one described in Gobat et al. (2015, hereafter G15) and we refer to that paper for additional information. However, we do not include an extended component to the fit, as done in G15, for two reasons: first, we are only interested here in the signal coming from the central galaxy; second, unlike for the star-forming centrals discussed in G15, the distribution of infrared flux originating from the galaxies' satellites is not easily modeled by a simple profile. As shown in Fig. 9, the SFR density of satellite candidates falls to the background level close to the central, hinting at a strong environmental effect. Therefore, we apply instead the clustering corrections of Béthermin et al. (2015, hereafter B15) to the measured fluxes, which were derived from simulations using the same COSMOS field. However, since B15 did not distinguish between galaxy types, we add an additional correction to the FIR bands to account for the increasing fraction of flux from satellites (Fig. 9) enclosed by the PACS, SPIRE, and SCUBA2 beams. This effectively raises the clustering corrections by up to a factor ~ 2 at $500 \mu\text{m}$. For both samples the stacked cutouts yield strong detections at $24 \mu\text{m}$ and 1.4 GHz. We also detect the total sample at 3σ in the SPIRE and SCUBA2 bands, and the low- z only at 250 and $350 \mu\text{m}$. The resulting SEDs are shown in Fig. 10.

We then fit the MIR to radio fluxes, including the upper limits, with two sets of dust emission models. We use the evolving Magdis et al. (2012, hereafter M12) main sequence and starburst templates (SB), and the models of Draine & Li (2007, hereafter DL07). For the latter, we set $q_{\text{PAH}} = 2.5\%$ and $U_{\text{max}} = 10^6$, but let U_{min} and γ vary. We also extend the models to the radio regime, assuming a power law slope with an index of $\alpha = 0.8$ and a normalization given by the FIR-radio correlation (Magnelli et al. 2015). The best-fitting models are shown in Fig. 10. With the MS template, we find $SFR_{\text{MS}} = 2.5 \pm 1.5$ (4.3 ± 1) $M_{\odot} \text{ yr}^{-1}$ for the low- z (respectively, total) sample. We integrate the dust SED (without radio slope) of the DL07 models between 8 and $1000 \mu\text{m}$ to estimate a total infrared luminosity of $L_{\text{IR}} = 1.3^{+1.2}_{-0.7}$ ($2.5^{+1.5}_{-0.9}$) $\times 10^{10} L_{\odot}$ for the low- z (respectively, total) sample, consistent with the absorbed luminosity $L_{\text{abs}} \sim 3 \times 10^{10} L_{\odot}$ in the UV, optical, and NIR, which we estimate from the best-fit model to the SED and the reddening curve between 90 \AA and $2.5 \mu\text{m}$ (see Capozzi et al. 2016, for details).

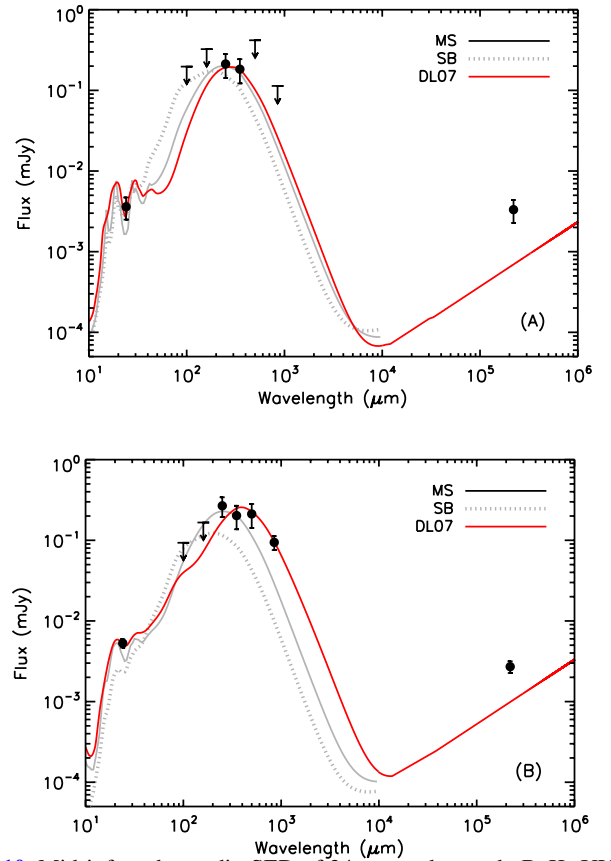


Fig. 10. Mid-infrared to radio SED of $24 \mu\text{m}$ -undetected pBzK+UVJp galaxies, in the low- z **A**) and total sample **B**), from stacked cutout images (filled circles with error bars, the arrows representing 3σ upper limits), with best-fit models from Magdis et al. (2012) (solid and dotted gray curves for main sequence and starburst templates, respectively) and Draine & Li (2007) (solid red curve extending to the radio regime). Both the M12 and DL07 models have been broadened according to the redshift distributions of each sample.

We convert L_{IR} into a SFR using the Kennicutt (1998) relation and find $SFR_{\text{DL07}} = 2.1^{+2.0}_{-1.0}$ ($4.1^{+2.5}_{-1.5}$) $M_{\odot} \text{ yr}^{-1}$, or 1.7 (1.5) dex below the MS at these redshifts. These values are in agreement with the total SFR inferred from the corrected line emission as well as with the values derived at $z \sim 1-1.5$ by M16 from *Herschel* data, both using samples of (differently-selected) quiescent galaxies. We also use the FIR SEDs and DL07 modeling thereof to estimate dust masses and temperatures, as well as gas masses for both samples. We present and discuss these results elsewhere (Gobat et al., in prep.).

5. Discussion

Our analysis suggests the presence of younger stellar populations in the outer regions of the pBzK galaxies in our sample compared to their cores. It provides a spectroscopic confirmation of the radial color gradients seen in resolved photometry of $z > 1$ ETGs (Guo et al. 2011; Gargiulo et al. 2012; Chan et al. 2016), and suggests that they arise at least in part from a radial age gradient. While the observed differences in the strength of the 4000 \AA break and the ratio of the Ca II H and Ca II K+H ϵ lines (Fig. 7) between the core (inner) and wings (outer) spectra could in principle also arise from a gradient in stellar metallicity, the presence of less metal-blended, high-order Balmer lines such as H δ offers a way to partially lift this degeneracy

(e.g., van Dokkum & Stanford 2003; Demarco et al. 2010). Consequently, the spectral modeling favors a younger stellar population in the galaxies' outskirts compared to their cores. This stellar population difference can be interpreted in different ways: on the one hand, this could be a signature of the recent accretion of low-mass satellites with younger stellar populations by this galaxy population. In this case, star formation would likely occur in extended or disk-like features (e.g., Appleton et al. 2014; Mancini et al., in prep.), consistent with our observations. Since this stellar population ratio is derived using a median spectrum, this would then imply that most of the galaxies contributing to the stack experienced such a rejuvenation episode during the last 1 Gyr.

On the other hand, it could be seen as tentative evidence for an inside-out quenching of star formation in these galaxies. This would be consistent with observations of depressed star formation in the inner regions of $z \gtrsim 2$ massive MS galaxies (Wuyts et al. 2013; Genzel et al. 2014; Tacchella et al. 2015), which are potential progenitors to the $z < 1.5$ ETGs. However, the young stellar population contributes only a relatively small fraction of the total stellar mass in either the core or wings. From the results of the spectral modeling, we can thus constrain the age gradient to be < 0.5 Gyr over ~ 6 kpc (~ 4 pixels) between the wings and core, respectively. This is a somewhat smaller value than would be expected from pure inside-out quenching (~ 2 Gyr over the same range for a $\sim 10^{11} M_{\odot}$ galaxy; e.g., Martig et al. 2009; Tacchella et al. 2015). It implies a faster quenching timescale (see, e.g., Onodera et al. 2015, for the case of $z \sim 1.6$ ETGs) and thus an additional quenching mechanism. Indeed, the apparent SFR deficit in close satellites of the pBzK+UVJp galaxies, as shown in Fig. 9, suggests that their immediate environment is efficient at suppressing star formation, providing further evidence that even at $z > 1$ the host halo could contribute an important quenching channel for high mass galaxies. Finally, we note that this small age gradient is of the same order as the ones observed in local massive ETGs (e.g., Spolaor et al. 2010; Kuntschner et al. 2010; Koleva et al. 2011; Barbosa et al. 2016), consistent with a mostly passive evolution to the present day.

We also detect [OII]3727 Å emission in the stacked spectrum. Although we have taken steps to remove AGN candidates from the stack, a low-ionization nuclear emission region (LINER) could still be a possible source for it, considering the nature of the sample (e.g., Yan et al. 2006). On the other hand, the [OII]3727 Å emission is distinctively more spatially extended than a point source, as shown in Fig. 8. We can thus interpret it as arising from low-level star formation consistent with the reconstructed SFH of the pBzK galaxies. Since we use a median stack, it is quite unlikely that this emission comes from separate but unresolved satellites rather than the galaxies themselves. If the age difference between the core and wings spectra is indeed a signature of inside-out quenching, one would expect the sSFR estimated from the line emission to be lower in the core than in the wings. However we cannot presently test this hypothesis: while the spatial profile of the line does appear to be slightly broader than the average K_s -band profile of the galaxies, suggesting a deficit of [OII]3727 Å emission per unit stellar mass in the core, the relatively low spatial resolution of both the broad-band image and our VIMOS spectra precludes an unambiguous comparison. Since our spectroscopic pBzK sample does not overlap with the CANDELS survey (Koekemoer et al. 2011), we do not have access to precise NIR morphologies for these galaxies nor, as a consequence, to truly resolved stellar mass information.

The SFR estimated from the [OII]3727 Å emission is consistent with both the stacked MIR and FIR emission from a larger sample of similarly-selected quiescent galaxies. This disagrees with the results of M16, who find that the SFRs derived from MIR fluxes are generally lower than the ones estimated from the FIR. Conversely, Fumagalli et al. (2014) conclude that the heating of cirrus dust by old stellar populations, rather than SFR, dominates the MIR emission of $z \sim 1.5$ quiescent galaxies by an order of magnitude. Similarly, Hayward et al. (2014) find that, in simulated quenched galaxies, L_{IR} tends to overestimate the true SFR by an order of magnitude for as long as 1 Gyr, due to residual heating of the dust by the last batch of stars. However, since the different indicators used here probe different timescales (a few tens of Myr in the case of line emission) the good agreement between SFR estimates derived from [OII]3727 Å and *Herschel* suggests that these alternative explanations are unlikely.

Finally, we note that the best-fit model underestimates the radio fluxes by a factor $\sim 3-5$ in both cases, which suggests the presence of low-level AGN activity in this sample (e.g., Sargent et al. 2010). The excess radio luminosity is $\sim 3 \times 10^{22}$ W/Hz, which falls well within the range dominated by low-excitation (radio-mode) AGNs (Best & Heckman 2012), even accounting for a non-zero spectral index (and therefore K-correction). This type of AGN is commonly found locally in massive red-sequence galaxies (e.g., Smolčić 2009) and associated with “maintenance mode” feedback, where the AGN outflow heats the surrounding extra-galactic medium, therefore preventing star formation. This excess is also present if we remove from the stack the cutouts that fall within the lower and upper 16 percentiles of the flux within a central aperture, thus removing potential biases from both negative noise peaks and detected radio sources. This would suggest that radio-mode feedback is pervasive up to at least $z \sim 1.8$, possibly playing a role in keeping the star formation rate low in these galaxies.

6. Summary

We present VLT/VIMOS spectroscopic observations of a sample of 35 massive B_zK -selected quiescent galaxies in the COSMOS field. We derive reliable redshifts for 31 sources, which we use together with available multiband photometry to estimate stellar masses and dust extinction values. Our sample has a median redshift of $z = 1.51$ and a median stellar mass of $1.1 \times 10^{11} M_{\odot}$ (Salpeter IMF). Our findings are summarized as follows:

- We create a median, spatially resolved 2D spectrum of the securely confirmed pBzK galaxies. We find that the outer part of this composite spectrum has features consistent with $f_{<1} \gtrsim 12\%$ of its stellar population being < 1 Gyr old, against $f_{<1} \lesssim 4\%$ in the inner part. This corresponds to an age difference of ≤ 0.4 Gyr over 6 kpc. We interpret this as possible evidence for either wide-spread rejuvenation episodes or an inside-out quenching process in these galaxies.
- We detect extended [OII]3727 Å emission consistent with residual star formation at a rate of $SFR_{\text{OII}} \sim 3-5 M_{\odot} \text{ yr}^{-1}$, after correcting for extinction, aperture, and slit losses.
- We perform stacked MIR, FIR, and radio photometry on a larger sample, which includes all galaxies in the COSMOS field in the same mass range that are selected as passive by both the B_zK and UVJ criteria and are undetected in the MIR. Our analysis yields FIR detections that allow us to derive a SFR_{IR} of $2-4 M_{\odot} \text{ yr}^{-1}$, consistent with the extinction-corrected value derived from the [OII]3727 Å emission. On

the other hand, we find radio fluxes a factor ~ 3 – 5 higher than predicted by the SFR, implying the widespread presence in the photometric sample of low-luminosity AGNs associated with maintenance-mode feedback.

- Given the median stellar masses of the spectroscopic and photometric samples, we find that quiescent galaxies at $z = 1.4$ – 1.8 have SFRs 1.5 – 1.7 dex below the MS at these redshifts. This is ~ 1 dex higher than the offset reported for local ETGs (~ -2.5 dex).

Acknowledgements. A.C. acknowledges the grant MIUR PRIN 2010–2011 “The dark Universe and the cosmic evolution of baryons: from current surveys to Euclid”. M.C. acknowledges support from a Royal Society University Research Fellowship, MTS from a Royal Society Leverhulme Trust Senior Research Fellowship. C.F. acknowledges funding from the European Union’s Horizon 2020 research and innovation programme under the Marie Skłodowska-Curie grant agreement No. 664931. GEM acknowledges support from the ERC Consolidator Grant funding scheme (project ConTExT, grant number No. 648179) and a research grant (13160) from Villum Fonden.

References

- Appleton, P. N., Mundell, C., Bitsakis, T., et al. 2014, *ApJ*, 797, 117
- Baldry, I. K., Balogh, M. L., Bower, R. G., et al. 2006, *MNRAS*, 373, 469
- Barbosa, C. E., Arnaboldi, M., Coccato, L., et al. 2016, *A&A*, 589, A139
- Belli, S., Newman, A. B., Ellis, R. S., et al. 2014, *ApJ*, 788, 29
- Best, P. N., & Heckman, T. M. 2012, *MNRAS*, 421, 1569
- Béthermin, M., Daddi, E., Magdis, G., et al. 2015, *A&A*, 573, A113
- Birnboim, Y., & Dekel, A. 2003, *MNRAS*, 345, 349
- Bruzual, G., & Charlot, S. 2003, *MNRAS*, 344, 1000
- Calzetti, D., Armus, L., Bohlin, R. C., et al. 2000, *ApJ*, 533, 682
- Capozzi, D., Maraston, C., Daddi, E., et al. 2016, *MNRAS*, 456, 790
- Carollo, C. M., Bschorr, T. J., Renzini, A., et al. 2013, *ApJ*, 773, 112
- Ceverino, D., & Klypin, A. 2009, *ApJ*, 695, 292
- Chan, J. C. C., Beifiori, A., Mendel, J. T., et al. 2016, *MNRAS*, 458, 3181
- Chiang, Y.-K., Overzier, R., & Gebhardt, K. 2014, *ApJ*, 782, 3
- Choi, J., Conroy, C., Moustakas, J., et al. 2014, *ApJ*, 792, 95
- Cimatti, A., Daddi, E., Mignoli, M., et al. 2002, *A&A*, 381, L68
- Cimatti, A., Daddi, E., Renzini, A., et al. 2004, *Nature*, 430, 184
- Citro, A., Pozzetti, L., Moresco, M., et al. 2016, *A&A*, 592, A19
- Croton, D. J., Springel, V., White, S. D. M., et al. 2006, *MNRAS*, 365, 11
- Daddi, E., Cimatti, A., Renzini, A., et al. 2004, *ApJ*, 617, 746
- Daddi, E., Renzini, A., Pirzkal, N., et al. 2005, *ApJ*, 626, 680
- Davidge, T. J., & Clark, C. C. 1994, *AJ*, 107, 946
- Dekel, A., & Birnboim, Y. 2006, *MNRAS*, 368, 2
- Demarco, R., Gobat, R., Rosati, P., et al. 2010, *ApJ*, 725, 1252
- Di Matteo, T., Springel, V., & Hernquist, L. 2005, *Nature*, 433, 604
- Donley, J. L., Koekemoer, A. M., Brusa, M., et al. 2012, *ApJ*, 748, 142
- Draine, B. T., & Li, A. 2007, *ApJ*, 657, 810
- Fanelli, M. N., O’Connell, R. W., Burstein, D., et al. 1990, *ApJ*, 364, 272
- Feldmann, R., & Mayer, L. 2015, *MNRAS*, 446, 1939
- Fumagalli, M., Labbé, I., Patel, S. G., et al. 2014, *ApJ*, 796, 35
- Gabor, J. M., Davé, R., Finlator, K., et al. 2010, *MNRAS*, 407, 749
- Gallazzi, A., Charlot, S., Brinchmann, J., et al. 2006, *MNRAS*, 370, 1106
- Gallazzi, A., Bell, E. F., Zibetti, S., et al. 2014, *ApJ*, 788, 72
- Gargiulo, A., Pérez, M. J., Cora, S. A., et al. 2012, *MNRAS*, 425, 2698
- Geach, J. E., Dunlop, J. S., Halpern, M., et al. 2017, *MNRAS*, 465, 1789
- Genzel, R., Förster Schreiber, N. M., Lang, P., et al. 2014, *ApJ*, 785, 75
- Gobat, R., Daddi, E., Onodera, M., et al. 2011, *A&A*, 526, A133
- Gobat, R., Strazzullo, V., Daddi, E., et al. 2012, *ApJ*, 759, 44
- Gobat, R., Strazzullo, V., Daddi, E., et al. 2013, *ApJ*, 776, 9
- Gobat, R., Daddi, E., Béthermin, M., et al. 2015, *A&A*, 581, A56
- Granato, G. L., De Zotti, G., Silva, L., et al. 2004, *ApJ*, 600, 580
- Guo, Y., Giavalisco, M., Cassata, P., et al. 2011, *ApJ*, 735, 18
- Hayward, C. C., Lanz, L., Ashby, M. L. N., et al. 2014, *MNRAS*, 445, 1598
- Hill, A. R., Muzzin, A., Franx, M., et al. 2016, *ApJ*, 819, 74
- Hopkins, P. F., Hernquist, L., Cox, T. J., et al. 2006, *ApJS*, 163, 50
- Kashino, D., Silverman, J. D., Rodighiero, G., et al. 2013, *ApJ*, 777, 8
- Kauffmann, G., White, S. D. M., Heckman, T. M., et al. 2004, *MNRAS*, 353, 713
- Kennicutt, R. C., Jr. 1998, *ARA&A*, 36, 189
- Koekemoer, A. M., Aussel, H., Calzetti, D., et al. 2007, *ApJS*, 172, 196
- Koekemoer, A. M., Faber, S. M., Ferguson, H. C., et al. 2011, *ApJS*, 197, 36
- Koleva, M., Prugniel, P., de Rijcke, S., et al. 2011, *MNRAS*, 417, 1643
- Krogager, J.-K., Zirm, A. W., Toft, S., et al. 2014, *ApJ*, 797, 17
- Kuntschner, H., Emsellem, E., Bacon, R., et al. 2010, *MNRAS*, 408, 97
- Kurk, J., Cimatti, A., Daddi, E., et al. 2013, *A&A*, 549, A63
- Le Floc’h, E., Aussel, H., Ilbert, O., et al. 2009, *ApJ*, 703, 222
- Lianou, S., Xilouris, E., Madden, S., et al. 2016, *MNRAS*, 461, 2856
- Lonoce, I., Longhetti, M., Saracco, P., et al. 2014, *MNRAS*, 444, 2048
- Lutz, D., Poglitsch, A., Altieri, B., et al. 2011, *A&A*, 532, A90
- Magdis, G., Daddi, E., Béthermin, M., et al. 2012, *ApJ*, 760, 6
- Magnelli, B., Ivison, R. J., Lutz, D., et al. 2015, *A&A*, 573, A45
- Man, A. W. S., Greve, T. R., Toft, S., et al. 2016, *ApJ*, 820, 11
- Mancini, C., Daddi, E., Renzini, A., et al. 2010, *MNRAS*, 401, 933
- Maraston, C., Strömbäck, G. 2011, *MNRAS*, 418, 2785
- Markwardt, C. B. 2009, *ASP Conf. Ser.*, 411, 251
- Martig, M., Bournaud, F., Teyssier, R., et al. 2009, *ApJ*, 707, 250
- McCarthy, P. J., Le Borgne, D., Crampton, D., et al. 2004, *ApJ*, 614, 9
- McCracken, H. J., Capak, P., Salvato, M., et al. 2010, *ApJ*, 708, 202
- McCracken, H. J., Milvang-Jensen, B., Dunlop, J., et al. 2012, *A&A*, 544, A156
- Mellier, Y., & Mathez, G. 1987, *A&A*, 175, 1
- Muzzin, A., Marchesini, D., Stefanon, M., et al. 2013, *ApJS*, 206, 8
- Newman, A. B., Ellis, R. S., Andreon, S., et al. 2014, *ApJ*, 788, 51
- Oliver, S. J., Bock, J., Altieri, B., et al. 2012, *MNRAS*, 424, 1614
- Onodera, M., Renzini, A., Carollo, M., et al. 2012, *ApJ*, 755, 26
- Onodera, M., Carollo, C. M., Renzini, A., et al. 2015, *ApJ*, 808, 161
- Peng, Y.-J., Lilly, S., Kovač, K., et al. 2010, *ApJ*, 721, 193
- Rettura, A., Rosati, P., Nonino, M., et al. 2010, *ApJ*, 709, 512
- Rettura, A., Mei, S., Stanford, S. A., et al. 2011, *ApJ*, 732, 94
- Salpeter, E. E. 1955, *ApJ*, 121, 161
- Sánchez-Blázquez, P., Peletier, R. F., Jiménez-Vicente, J., et al. 2006, *MNRAS*, 371, 703
- Sargent, M. T., Schinnerer, E., Murphy, E., et al. 2010, *ApJS*, 186, 341
- Sargent, M. T., Daddi, E., Béthermin, M., et al. 2014, *ApJ*, 793, 19
- Sargent, M. T., Daddi, E., Bournaud, F., et al. 2015, *ApJ*, 806, 20
- Schinnerer, E., Sargent, M. T., Bondi, M., et al. 2010, *ApJS*, 188, 384
- Scodreggio, M., Franzetti, P., Garilli, B., et al. 2005, *PASP*, 117, 1284
- Scoville, N., Aussel, H., Brusa, M., et al. 2007, *ApJS*, 172, 1
- Serven, J., Worthey, G., Toloba, E., et al. 2011, *AJ*, 141, 184
- Shetty, S., & Cappellari, M. 2015, *MNRAS*, 454, 1332
- Smolčić, V. 2009, *ApJ*, 699, 43
- Spitler, L. R., Labbé, I., Glazebrook, K., et al. 2012, *ApJ*, 748, 21
- Spolaor, M., Kobayashi, C., Forbes, D. A., et al. 2010, *MNRAS*, 408, 272
- Strazzullo, V., Daddi, E., Gobat, R., et al. 2015, *A&A*, 576, L6
- Tacchella, S., Carollo, C. M., Renzini, A., et al. 2015, *Science*, 348, 314
- Tanaka, M., Toft, S., Marchesini, D., et al. 2013, *ApJ*, 772, 113
- Thomas, D., Maraston, C., Bender, R., et al. 2005, *ApJ*, 621, 673
- Thomas, D., Maraston, C., Schawinski, K., et al. 2010, *MNRAS*, 404, 1775
- van Dokkum, P. G., & Stanford, S. A. 2003, *ApJ*, 585, 78
- van Dokkum, P. G., Franx, M., Kriek, M., et al. 2008, *ApJ*, 677, 5
- Vazdekis, A., Sánchez-Blázquez, P., Falcón-Barroso, J., et al. 2010, *MNRAS*, 404, 1639
- Wagner, C. R., Brodwin, M., Snyder, G. F., et al. 2015, *ApJ*, 800, 107
- Whitaker, K. E., van Dokkum, P. G., Brammer, G., et al. 2013, *ApJ*, 770, 39
- Williams, R. J., Quadri, R. F., Franx, M., et al. 2009, *ApJ*, 691, 1879
- Williams, C. C., Giavalisco, M., Bezanson, R., et al. 2017, *ApJ*, submitted [arXiv:1607.06089]
- Woo, J., Dekel, A., Faber, S. M., et al. 2015, *MNRAS*, 448, 237
- Wuyts, S., Förster Schreiber, N. M., Nelson, E. J., et al. 2013, *ApJ*, 779, 135
- Yan, R., Newman, J. A., Faber, S. M., et al. 2006, *ApJ*, 648, 281

Appendix A: Spectroscopic redshifts

Table A.1. Spectroscopic redshifts of the pBzK galaxies in our sample.

ID	RA (deg)	Dec (deg)	z_{spec}	Quality
206 430	150.00462	2.47327	1.4595	A
207 538	150.01192	2.48666	1.5499	A
208 020	150.04401	2.49370	1.9677	B ⁻
211 123	150.04243	2.52651	1.0296	C
214 127	150.09035	2.56794	1.9677	B
218 368	150.09189	2.61840	1.6658	B ⁻
219 830	150.09418	2.63460	1.3965	A
220 268	150.01241	2.64065	2.0892	B
221 046	150.04456	2.65100	1.4408	A
221 493	150.00569	2.65488	1.2471	A
222 897	150.01764	2.67258	1.5839	A
223 635	150.00270	2.67492	1.2468	A
223 796	149.98267	2.68305	1.4372	A
225 039	150.08479	2.69475	1.3005	A
225 317	150.10361	2.69767	1.4072	A
226 037	150.08859	2.70642	1.3770	C
220 655	150.00571	2.64554	0.8938	B
221 824	150.01912	2.65889	1.3961	A
226 380	150.09518	2.71000	1.4122	B
248 681	149.89543	2.62726	1.5596	A
248 881	149.81070	2.63236	1.5199	A
250 123	149.86220	2.64795	1.5681	B
250 513	149.82225	2.65310	2.0799	B
252 409	149.86949	2.67430	1.4050	A
254 526	149.80560	2.70258	1.5126	A
254 313	149.87495	2.69825	1.3149	A
236 990	149.88060	2.48648	1.5519	A
238 164	149.89635	2.49910	1.5642	A
240 680	149.83612	2.52852	1.6587	C
243 072	149.89896	2.55742	1.5888	B
243 201	149.89194	2.56043	1.5939	A
243 731	149.82497	2.56692	1.5145	B
237 270	149.85873	2.48966	1.8368	B
241 810	149.85217	2.54303	1.1757	A

Appendix B: Stellar population properties

Table B.1. Results of the spectral modeling for the different types of spectral decomposition (Col. 1) and models (Col. 2).

		$f_{<1,\text{core}}$ (%)	$f_{<1,\text{wings}}$ (%)	Age _{core} (Gyr)	Age _{wings} (Gyr)
Gaussian	V10	3 ± 1	13 ± 1	2.8 ± 0.1	2.4 ± 0.3
	M11	4 ± 1	21 ± 7	2.9 ± 0.1	2.7 ± 0.3
de Vaucouleurs	V10	3 ± 1	12 ± 2	2.8 ± 0.1	2.4 ± 0.3
	M11	3 ± 1	18 ± 6	2.9 ± 0.7	2.7 ± 0.9

Notes. Column (3) and (4): fraction of stars with ages <1 Gyr in the core and wings, respectively; Cols. (5) and (6): mass-weighted average age of the core and wings, respectively.